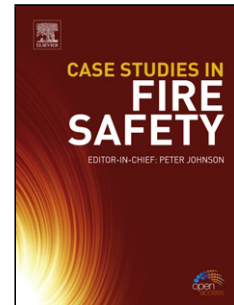


Accepted Manuscript

Title: Influence of microstructure on the corrosion of archaeological iron observed using 3D synchrotron micro-tomography

Authors: H.J. Simon, G. Cibin, C. Reinhard, Y. Liu, E. Schofield, I.C. Freestone



PII: S0010-938X(19)30244-6
DOI: <https://doi.org/10.1016/j.corsci.2019.108132>
Article Number: 108132

Reference: CS 108132

To appear in:

Received date: 1 February 2019
Revised date: 13 July 2019
Accepted date: 30 July 2019

Please cite this article as: Simon HJ, Cibin G, Reinhard C, Liu Y, Schofield E, Freestone IC, Influence of microstructure on the corrosion of archaeological iron observed using 3D synchrotron micro-tomography, *Corrosion Science* (2019), <https://doi.org/10.1016/j.corsci.2019.108132>

This is a PDF file of an unedited manuscript that has been accepted for publication. As a service to our customers we are providing this early version of the manuscript. The manuscript will undergo copyediting, typesetting, and review of the resulting proof before it is published in its final form. Please note that during the production process errors may be discovered which could affect the content, and all legal disclaimers that apply to the journal pertain.

Influence of microstructure on the corrosion of archaeological iron observed using 3D synchrotron micro-tomography

H. J. Simon,^{1,2*} G. Cibin,² C. Reinhard,² Y. Liu,¹ E. Schofield,³ I. C. Freestone¹

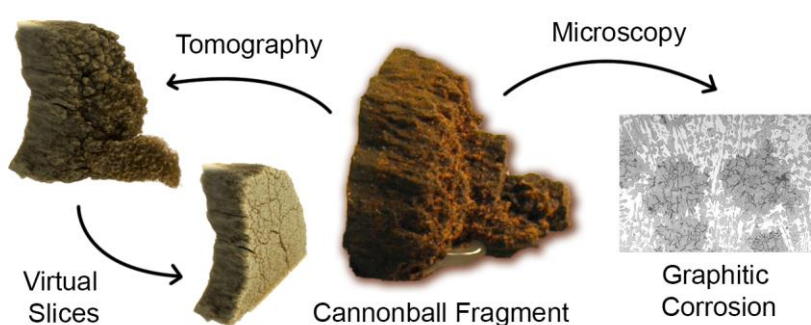
¹ UCL Institute of Archaeology, 31-34 Gordon Square, London, WC1H 0PY, UK

² Diamond Light Source, Harwell Campus, Didcot, Oxfordshire, OX11 0DE, UK

³ The Mary Rose Trust, College Road, HM Naval Base, Portsmouth, PO1 3LX, UK

* Hayley.simon.15@ucl.ac.uk

Graphical abstract



Highlights

- Corrosion in cast iron cannon shot fragment not directly co-located with cracks
- Akaganeite occurs selectively around graphite flakes in microstructure
- Graphite acts as local, rather than global, cathode
- Formation of akaganeite occurred post-conservation

Abstract

A combination of X-ray analytical techniques has been used to study the microstructure and corrosion of a 450-year-old cast-iron cannonball fragment from the *Mary Rose* shipwreck. Using a 3D approach, it has been shown that akaganeite, $\beta\text{-FeO}(\text{OH}, \text{Cl})$, starts to appear ~ 1.5 mm below the outer surface of the object, occurring selectively around non-contiguous graphite flakes in the microstructure, with no corrosion in graphite-free regions. This spatial analysis has given a new look inside a 450-year-old system, to see how metallographic features interact with local chemical environments to give complex corrosion products, centuries in the making.

Key words: Tomography, cast iron, graphite, conservation, archaeology, *Mary Rose*

Introduction

A detailed understanding of how metallographic properties influence the corrosion of archaeological iron is vital in the development of more effective, tailored conservation strategies. While countless studies have looked at the microstructure of historic iron alloys, or the structure of corrosion layers, only a handful have studied the corrosion products alongside the metallography [1–3] and fewer have formed a direct link between the corrosion process and the alloy composition. [4] In contrast, for modern metals, much has been achieved to relate microstructure properties to the corrosion, from the impact of inclusions on pitting corrosion, [5] to the inhibition effect of alloying elements. [6] However, conclusions based on modern alloys cannot be directly applied to archaeological material. Each corrosion-reducing advance takes the behaviour of a modern metal further away from its archaeological counterpart. As a result, to understand how corrosion proceeds in a historic alloy, investigations must characterise both the metal microstructure and corrosion products concurrently.

One of the most challenging metals for conservation is iron. Archaeological iron typically originates from one of two smelting processes: a *direct* process [7] that produces a solid bloom of wrought iron in the form α -ferrite (α -Fe); or an *indirect* process, [8] which forms a molten, liquid iron-carbon alloy that may be directly cast into a mould, giving a cast iron, or which can be decarburised to form a wrought iron. While both methods produce iron that is susceptible to corrosion, the mechanism is likely to be different for cast and wrought irons due to the differing carbon content of the alloy. It has been recognised that this variation requires a different conservation approach, [9,10] particularly in the case of marine iron, [9] however it is less clear how the species of carbon – e.g. cementite (Fe_3C) in a white cast iron, or graphite (C) in a grey cast iron – influences the corrosion and subsequent conservation of archaeological iron.

Corrosion of archaeological iron has been found to be accelerated by the presence of chloride ions, Cl^- , [11] which present a significant issue for objects excavated from chlorine-rich environments, such as marine burials. [1] To address this, conservation treatments for archaeological iron focus on removal of chlorine from the artefact. [12,13] A recent investigation into the impact of conservation on cast iron corrosion [14] noted severe structural degradation to cast iron cannon shot from the *Mary Rose* shipwreck (c. 1545) following a washing-based conservation treatment. Using a destructive sampling methodology, [15] it was concluded that this mechanical damage occurred during object storage and display, arising from corrosion around cracks and casting voids inside the artefact. [14,15] Previous studies on the corrosion

of iron in indoor atmospheric conditions have shown that in the presence of Cl^- the iron oxyhydroxide akaganeite, $\beta\text{-FeO}(\text{OH}, \text{Cl})$, may form around cracks. [16–18] However, as these investigations focused on the interaction of metal with external environments, the cracks studied were restricted to the corrosion layer [16,17] or surrounding medium, [19] rather than inside the metal object itself. After undergoing a conservation treatment, the outer surface of an iron artefact is typically coated with a protective layer – a wax-graphite mixture for cast irons and a phosphate-based primer for wrought irons [9] – meaning there is limited interaction between the metal surface and the external environment. However, damage is visually observed to occur due to corrosion and fracturing inside the object, made apparent by eventual breakage of the fragment from the surface of the shot. This suggests the structure below the corrosion layer is likely to be paramount to the corrosion mechanism. To gain a better insight into the relationship between corrosion, metal microstructure and the local internal environment, a spatial analysis must be performed. This can only be achieved using a three-dimensional approach.

Tomographic analyses create a 3D representation of a sample by building a series of 2D cross-sectional slices. Individual cross-sections may consist of X-radiographs, [20] diffraction patterns, [21] neutron radiographs [22] or spectroscopic data [21] depending on the material and system being studied. The most common tomography, X-ray computed tomography (CT), has been shown to be a highly effective non-destructive method for studying archaeology, [23–25] corrosion [19,26,27] and metallography [28,29], particularly when used in combination with 2D analytical methods. In the present work, the relationship between cracks, corrosion and metal microstructure in archaeological cast iron is investigated through analysis of a fragment of a 450-year-old cast iron shot, which has been subjected to known conservation treatments over 3 decades, by synchrotron X-ray micro-computed tomography ($\mu\text{-CT}$) in combination with microscopy and chemical characterisation of the corrosion products by synchrotron X-ray powder diffraction (SXPd) and X-ray Absorption Near Edge Spectroscopy (XANES).

Materials and Method

Archaeological background

Cast iron first appeared in China in the 5th century B.C., where it was typically used for mass-produced agricultural tools. [30] In contrast, in Europe the earliest evidence of blast furnace use dates from the 11th century, although, until the 14th century, the furnace products were only used for conversion into wrought iron. [8] It is widely accepted that the first blast furnace in England began operation in 1496 in Newbridge, Sussex in the Weald. [31,32] Unlike the earlier European blast furnaces, the Wealden furnace was constructed, in part, to make

castings directly from the initial melt. This enabled a quick and cheap method of producing a large numbers of projectiles. [33] In particular, cast iron was used alongside stone and lead to make cannon shot for warships. The largest collection of Tudor cannon shot in the UK comes from the excavation of King Henry VIII's flagship, the *Mary Rose*, which sunk off the coast of Portsmouth on 19th July 1545. More than 1,200 individual cast iron shot were recovered from the shipwreck between 1979 and 1983, [34] and over the past 35 years, various conservation treatments have been applied in an effort to minimise corrosion.

Shot Conservation History

A fragment, approx. 13 (L) x 8 (W) x 9 (H) mm, of *Mary Rose* cannon shot number 81A6143, **Fig. 1**, was collected for μ -CT. The artefact was excavated in 1981 from the ship's Bow side shot store, situated on the main deck, as a concretion. At the time of excavation, the shot had dimensions: weight, $w = 1713$ g and diameter, $d = 86$ mm. Following excavation, the shot was passively stored in an alkaline solution, an established method of passivating marine archaeological iron after excavation. [35] From 1981 this solution comprised NaOH (0.13 M, pH 12) but in 2007 it was changed to an equimolar mixture of Na₂CO₃/NaHCO₃ (0.15 M, pH 10). The shot remained in passive storage solution until December 2010, when it was taken for interventive conservation. Once removed from the Na₂CO₃/NaHCO₃ solution, the shot was rinsed in tap water, then washed in 3 consecutive baths of a 2% v:v solution of the corrosion inhibitor Hostacor® IT, [36] **Scheme 1**, in tap water. This treatment was designed as a neutral pH wash to remove Cl⁻ via a diffusion mechanism. [37] The shot was immersed in the first 2 washing baths for 2 days and the final bath for 2 weeks. On completion of the final wash, the shot was dried in a 2-stage acetone:water (1:1 and 1:0) series before being coated in wax and placed in environmentally controlled storage.

On the conservation record it was noted that visible cracks were forming, and the shot was returned to the conservation lab in February 2011. The wax coating was removed and the Hostacor:water washing treatment repeated, with 3 baths lasting 2.5, 4 and 6 weeks. Following the second set of Hostacor:water washing, the shot underwent an alkaline sulphide reduction treatment, [38] which involved washing the shot in a solution of 0.1 M NaOH/0.05 M Na₂SO₄ (pH 12-13) at 45 °C. The alkaline sulphide reduction treatment was completed in November 2012, at which time the shot was dried at 50 °C and coated in wax. It was eventually put on display in the *Mary Rose* museum in early 2013. In July 2013, nearly 300 shot, including this one, were taken off display and placed in controlled storage (20 °C, 20% RH), as damaging corrosion was observed in all the shot that had been through a soaking treatment. The outside of the artefact began to peel off the central core of the ball, giving a large number of fragments

and a remaining core with $d \approx 80$ mm, as shown in **Fig. 1-a** and **1-c**. One fragment, **Fig. 1-b**, was mounted on a 25 mm sample holder and imaged by μ -CT in October 2017.

3D Representation

Tomography experiments were carried out at the Joint Engineering, Environmental, and Processing (JEEP) beamline I12 at Diamond Light Source, Didcot, UK. [39] μ -CT was performed using a monochromatic X-ray beam (100 keV), using a PCO.edge CMOS imaging camera (2560 x 2160 pixel, 16-bit depth) across an imaging area of 20 x 12 mm, with a pixel resolution of 7.9 μ m per pixel. 1800 projections were recorded over 180° rotation, with an exposure time of 0.007 s. 2D radiographs were reconstructed using the *SAVU* reconstruction pipeline [40] developed at Diamond Light Source, using a standard filtered back-projection algorithm and exported as a stack of 1901 TIFF images (2560 x 2560 pixels). One image from the stack, image 202, was used to investigate the change in corrosion spot area using the Analyze Particles feature of *ImageJ*. [41] The entire image stack, see **SI Movie 1**, was opened in *ImageJ*, compressed to 8-bit greyscale, cropped and reduced in size to give a (337 x 519 x 444) image stack ahead of volume rendering using the software *Drishiti*. [42] Segmentation of the metal, cracks, corrosion and wax volumes was performed in *DrishitiPaint*. The background was removed by shrink-wrapping the reconstructed volume and closing holes <10 px in size. After removing the background, the 4 features were then differentiated via their grayscale values and a percentage volume calculated from the segmented voxels.

Metallographic Analysis

Following μ -CT analysis, the sample was removed from the sample holder and prepared for metallographic analysis. The fragment was mounted in a 2-part bisphenol A epichlorohydrin epoxy resin (MetPrep, Coventry, UK), vacuum impregnated and ground with a series of SiC abrasive discs (grades 320-4000, grain size 40-5 μ m). The surface was polished using diamond paste (grain size 3 and 1 μ m) and carbon coated prior to analysis using a Hitachi S-3400N scanning electron microscope (Hitachi High-Technologies, Maidenhead). Images were collected in back scatter electron mode with an accelerating voltage of 20 kV, collection time of 160 s and a resolution of 2560 x 1920.

Chemical Characterisation of Corrosion Products

A second sample that had peeled off the central core of shot 81A6143 was collected, ground to a fine powder in an agate pestle and mortar and mounted in a 0.5 mm quartz capillary (Capillary Tube Supplies Ltd, Cornwall, UK) in a brass capillary holder secured with a cyanoacrylate adhesive (RS Components Ltd., Corby, UK). The capillary sample was placed in the high-resolution powder diffraction beamline, I11, at Diamond Light Source, where SXP

measurements were performed using 5 multi-analysing crystal (MAC) detectors, $\lambda = 0.82578 \text{ \AA}$ (calibrated with NIST SRM640c Si standard) [43] at room temperature and pressure, with an exposure time of 1800 s. Following data collection, phase identification was performed using the software *QUALX2*, [44] by comparing the experimental pattern to the crystallography open database (COD). Approximate phase proportions were calculated in *QUALX2* based on the Reference Intensity Ratio, I/I_c (c = corundum) method, [45] accuracy $\pm 5 \text{ wt\%}$.

An additional sample was cut from the remaining metal core using a hacksaw fitted with a stainless-steel blade, 24 teeth per inch (tpi) for Cl k-edge XANES analysis. The cut cross-section was mounted in a 2-part polyester resin (MetPrep, Coventry, UK) as a 25 mm circular block. The surface of the cross-section was covered by a layer of resin until arrival at the core EXAFS beamline, B18, at Diamond Light Source, to prevent corrosion between sampling and analysis. On arrival at the beamline, the outer resin layer was removed by grinding dry with a series of SiC abrasive discs (grades 240, 400, 800 and 1200). Between grades the sample was dusted with compressed N_2 and on completion of final grade, the exposed sample was placed in a sealed plastic box flushed with N_2 before being mounted in a custom 3D-printed sample holder on the beamline. The sample, detector and beam were enclosed in a plastic bag flushed with He. The beamline optics used Cr coated collimating and focusing mirrors, a Si(111) monochromator and Ni coated harmonic rejection mirrors. The first ion chamber (I_0) was filled with He gas. The spot size of the beam was $\sim 100 \times 100 \text{ \mu m}$. Cl k-edge XANES spectra were collected in fluorescence mode using a 4 element Vortex Si drift detector in the energy range 2722-3200 eV with steps of 0.2 eV. The data set was processed using previously published methodology and Cl standards. [14]

Results and Discussion

Cast iron that pre-dates the industrial revolution, [8,30,46] may be characterised as either *white* or *grey*, depending on the form of carbon present in the metal. Which type forms is determined by the cooling rate and composition of the melt. In a white cast iron, carbon is present as iron carbide (Fe_3C), giving a hard, brittle metal, while in a grey cast iron the carbon forms graphite flakes, creating a softer, more fluid alloy that may be readily cast into intricate shapes. [47] Typically, grey cast irons are produced using a slower cooling rate than white cast irons, which allows graphite flakes to precipitate during the casting process. If a temperature gradient occurs during cooling, carbon may present as both Fe_3C and graphite, with differing ratios across the object. In cases where both graphite and Fe_3C form, the alloy is referred to as a mottled cast iron. Metallographic examination of one *Mary Rose* shot performed in 2002, [33] showed that the microstructure on the outer surface consists of ledeburite – pearlite (lamellar α -Fe and Fe_3C) in a cementite (Fe_3C) matrix – changing to a

structure of graphite flakes in a ledeburite matrix towards the centre of the casting. This microstructure is consistent with a fast cooling rate on the outside and slower cooling on the inside. [33,34] This difference in cooling speed is also observed in the fragment of shot 81A6143. For example, in the tomographic slice shown in **Fig. 2** differences in the greyscale shade arise from the X-ray attenuation of the material, with complete attenuation giving a white appearance – a value of 255 in 8-bit greyscale – and no attenuation a black appearance – value 0 in 8-bit greyscale. In the shot fragment, the highest attenuation comes from the metallic areas of the sample, giving a lighter shade (value ~160), whereas less attenuation occurs from the iron oxide corrosion products, resulting in a darker grey (value ~115) and the cracks appear darkest (value ~80) due to the absence of material. In **Fig. 2**, moving from the outer surface of the fragment – identifiable by the applied wax layer – towards the inside of the casting, the grain size increases, **Fig. 2 insets**, resulting in a structure that may be described as a white to mottled cast iron.

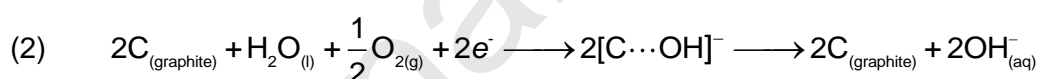
Alongside this increase in grain size, the corroded areas, which appear as dark grey, circular spots, increase in radius deeper into the casting, **Fig. 3**. In total, 147 corrosion spots were resolved by the area analysis method, as outlined in **Fig. 3-a**, giving areas ranging from 0.010 to 0.152 mm², with an average of 0.033 mm² and standard deviation 0.026 mm². Examination of the corroded areas with an electron microscope, **Fig. 4**, reveals that corrosion is related to the presence of graphite in the metal microstructure. This is consistent with corrosion around kish graphite that has a larger size towards the centre of the casting due to a slower cooling rate. [48] The microstructure on the outer, white cast iron, surface of the fragment consists only of ledeburite and no graphite is present.

Correspondingly, across the whole tomographic series, **SI Movie 1**, corrosion products consistently do not appear until ~1.5 mm below the outer surface. 3D reconstruction of the μ -CT data, **Fig. 5** and **SI Movies 2 and 3** show that as the sample progresses from the wax coating (**Fig. 5** top left) to the point that was once in contact with the remaining core of the shot (**Fig. 5** bottom right), corrosion products [dark brown spots] start to appear with increasing frequency and volume. Interestingly, although cracks [black lines] are present throughout the sample, corrosion products are not co-located with cracks.

To investigate how each feature present in the sample varies spatially, a segmentation procedure was developed that differentiates the metal (grey), cracks (pink), corrosion (blue) and wax (green) volumes, **Fig. 6-a** based on their greyscale value. It should be noted that the greyscale values of the cracks and corrosion features overlap – for example in **Fig. 3-a** two

crack areas were incorrectly identified as corrosion spots, highlighted by pink arrows – making it challenging to fully differentiate the two features. This uncertainty has been reflected in the volume analysis in **Fig. 6-b** by a larger error associated with the cracks and corrosion than the metal and wax. Splitting the shot fragment into 3 sections, representing the outer region, the middle region and the internal region that was once in contact with the rest of the artefact, the percentage volume of the metal decreases, while the cracks and corrosion volumes increase deeper into the casting. This is consistent with the 2D analysis of the sample. Furthermore, comparison of the segmented cracks and corrosion features show that, while both increase with depth into the fragment, their locations are not directly associated with one another, but rather the increase in corrosion leads to greater mechanical stresses and cracking, resulting in a global increase in cracks. Instead of being associated with cracks, the appearance of corroded areas is closely related to the presence of graphite in the metal microstructure.

Selective corrosion around graphite in grey cast iron is a known form of dealloying corrosion, commonly referred to as graphitic corrosion. [47,49–52] It has been demonstrated that in an acidic solution – the environment commonly observed inside a metal crevice – graphite acts as a net cathode [53] to metal corrosion; oxidation of the α -Fe phase **(1)**. The graphite itself is not reduced during the reaction, but instead provides favourable oxygen reduction reaction **(2)** kinetics, [54,55] resulting in a localised increase in the corrosion rate. Graphite can further act as an electron conductor in the corrosion process, providing an additional increase in the reaction kinetics.



In the presence of graphite, stainless steel has been shown to corrode at double the rate when compared to a system with no graphite present, and forms larger voids in the metal. [56] The initially proposed model of graphitic iron corrosion suggested that the process may only occur if a continuous network of graphite is present in the alloy [47,49] and would not be observed if graphite forms isolated nodules or flakes. The graphite found in the *Mary Rose* cannon shot investigated in this work does not form a continuous network and occurs instead as isolated flakes. Yet preferential corrosion around graphite is still observed, **Fig. 4**. This means a continuous graphite network is not necessary for graphitic corrosion to occur. As a result, it may be concluded that the localised increase of oxygen reduction kinetics on graphite plays a more important role in increasing the overall corrosion rate than the global effect of increased

conductivity from a graphite network. However, this is a simplification as it does not consider the role of chlorine and other salts present in the environment.

To better understand the corrosion reaction that occurred inside the shot, a chemical characterisation of the corrosion products was performed. A second fragment of shot 81A6143 from the same area of the object as the sample used for tomography was ground to a fine powder and analysed by SXPD, **Fig. 7**, to characterise the crystalline phases present. The diffraction results support the metallographic analysis, where the predominant phase is Fe_3C with some graphite in the sample. The only corrosion product identified was the chlorinated iron oxyhydroxide, akaganeite, $\beta\text{-FeO}(\text{OH}, \text{Cl})$. Akaganeite has a crystal structure stabilised by chloride, [57] and can form only if chlorine (or fluorine) is present in the system. [58] As a result, identification of $\beta\text{-FeO}(\text{OH}, \text{Cl})$ below the surface of the object means that chloride must have been available for reaction inside the shot during corrosion.

Within the akaganeite crystal, two chlorine sites are present: partially bound chloride adsorbed to the surface of the crystal, Cl_{sur} , and structurally bound chloride within the tunnel structure of the crystal, Cl_{str} . [59] Earlier work has shown that these two sites may be differentiated by X-ray Absorption Spectroscopy, [14,59] which is particularly useful for studies of iron post-conservation, as only one site – the mobile Cl_{sur} – is thought to be removed during a washing based conservation treatment. [57,59,60] Loss of Cl_{sur} during aqueous washing may be observed by a decrease in the pre-edge feature in the akaganeite Cl k-edge XANES. [14] This is illustrated in **Fig. 8-a** for a lab-synthesised akaganeite standard immediately after synthesis (red), where a pre-edge can be seen, and following 1 month of washing in dH_2O (blue), where the pre-edge has been lost. In the XANES spectrum of the akaganeite from shot 81A6143, **Fig. 8-b** (green), a pre-edge feature is observed. This indicates Cl_{sur} is present in the crystal. If it is assumed that the conservation procedures applied to the shot have a similar effect to washing of the standard, i.e: removal of surface bound Cl_{sur} , these results suggest that akaganeite from shot 81A6143 did not go through the conservation treatment. Instead, the phase likely formed after treatment, while the object was in storage. For akaganeite to form inside the object post-conservation, Cl, oxygen and water must have been available for reaction in internal areas of the shot, transported via the crack network. This chlorine may either have originated from the tap water used to prepare the treatment solutions, or from residual Cl not removed during conservation. As a result, although the corrosion reaction is localised to graphite sites, it would not have been able to proceed without the local environment created by the transport network of the cracks.

Conclusions

In this work, a powerful suite of techniques has been used to understand the 3D process of corrosion in marine archaeological iron. The results indicate that the corrosion process of a cast iron is dependent upon microstructure and phase composition, which are controlled by the smelting conditions and elemental composition of the alloy. The outer ~1.5 mm of the *Mary Rose* cannonball investigated comprises of α -Fe and Fe₃C and shows no corrosion. However, below 1.5 mm, graphite is developed, and corrosion has occurred preferentially around the graphite, frequently causing exfoliation of the outer surface. The graphite is present as isolated flakes, meaning the continuous graphite network assumed necessary in previous corrosion models was not present. This implies that graphite is acting as a local, rather than a global cathode.

The main corrosion product, the chlorinated iron oxyhydroxide, akaganeite, appears to have formed after conservation was performed to mitigate corrosion of the artefact. As this phase forms only in the presence of chlorine, it may be concluded that corrosive species were transported to the interior of the artefact during or after treatment. This is likely to have been primarily via the network of cracks present throughout the sample, causing corrosion below the surface of the ball, leading to further cracking and eventual fracturing of the object. To alleviate this, during conservation, care should be taken to avoid contact with fluids such as tap water, which practitioners may not be aware has an intrinsic concentration of chlorine.

Acknowledgements

The work presented in this paper is co-funded by the UK's Engineering and Physical Sciences Research Council (EPSRC) and Diamond Light Source as part of the Centre for Doctoral Training in Science and Engineering in Arts, Heritage and Archaeology (SEAHA-CDT). The authors wish to thank Professor Mary Ryan, Dr Alexandra Hildred, Dr Sarah Day, Dr Chiu Tang, Mr Phil Robbins, Mr Ole Nordland, Mr Robert Turner and Dr John Merkel for their helpful contributions to this project.

References

- [1] C. Rémazeilles, D. Neff, F. Kergourlay, E. Foy, E. Conforto, E. Guilminot, S. Reguer, P. Refait, P. Dillmann, Mechanisms of long-term anaerobic corrosion of iron archaeological artefacts in seawater, *Corros. Sci.* 51 (2009) 2932–2941. doi:10.1016/j.corsci.2009.08.022.
- [2] D. Cvikel, E.D. Mentovich, D. Ashkenazi, Y. Kahanov, Casting techniques of cannonballs from the Akko 1 shipwreck: Archaeometallurgical investigation, *J. Min. Metall. Sect. B Metall.* 49 (2013) 107–119. doi:10.2298/JMMB120216022C.
- [3] M. Hernandez, M. Hernandez-Escampa, C. Abreu, J. Uruchurtu, M. Bethencourt, A.

- Covelo, Characterization of a Historical Cannonball from the Fortress of San Juan De Ulúa Exposed to a Marine Environment, *Archaeometry*. 58 (2016) 610–623. doi:10.1111/arc.12194.
- [4] R. Balasubramaniam, On the corrosion resistance of the Delhi iron pillar, *Corros. Sci.* 42 (2000) 2103–2129.
- [5] M.P. Ryan, D.E. Williams, R.J. Chater, B.M. Hutton, D.S. McPhail, Why stainless steel corrodes, *Nature*. 415 (2002) 770–774.
- [6] C.A. Olsson, D. Landolt, Passive films on stainless steels - chemistry, structure and growth, *Electrochim. Acta*. 48 (2003) 1093–1104. doi:10.1016/S0013-4686(02)00841-1.
- [7] R. Pleiner, *Iron in Archaeology: The European Bloomery Smelters*, Archeologicky ustav AV CR, Praha, 2000.
- [8] P.T. Craddock, Cast Iron, Fined Iron, Crucible Steel: Liquid Iron in the Ancient World, in: P.T. Craddock, J. Lang (Eds.), *Min. Met. Prod. through Ages*, British Museum, London, 2003: pp. 231–257.
- [9] N.A. North, Conservation of Metals, in: C. Pearson (Ed.), *Conserv. Mar. Archaeol. Objects*, Butterworths, London; Boston, 1987: pp. 207–252.
- [10] M. Rimmer, D. Thickett, D. Watkinson, H. Ganiaris, *Guidelines for the Storage and Display of Archaeological Metalwork*, English Heritage, Swindon, 2013.
- [11] M. Rimmer, D. Watkinson, Q. Wang, The impact of chloride desalination on the corrosion rate of archaeological iron, *Stud. Conserv.* 58 (2013) 326–337.
- [12] N.A. North, C. Pearson, Washing Methods for Chloride Removal from Marine Iron Artifacts, *Stud. Conserv.* 23 (1978) 174–186. doi:10.1179/sic.1978.023.
- [13] S. Turgoose, The corrosion of archaeological iron during burial and treatment, *Stud. Conserv.* 30 (1985) 13–18.
- [14] H. Simon, G. Cibir, P. Robbins, S. Day, C. Tang, I. Freestone, E. Schofield, A Synchrotron-Based Study of the Mary Rose Iron Cannonballs, *Angew. Chemie - Int. Ed.* 57 (2018) 7390–7395. doi:10.1002/anie.201713120.
- [15] E.J. Schofield, Illuminating the past: X-ray analysis of our cultural heritage, *Nat. Rev. Mater.* (2018). doi:10.1038/s41578-018-0037-4.
- [16] D. Neff, L. Bellot-Gurlet, P. Dillmann, S. Reguer, L. Legrand, Raman imaging of ancient rust scales on archaeological iron artefacts for long-term atmospheric corrosion mechanisms study, *J. Raman Spectrosc.* 37 (2006) 1228–1237. doi:10.1002/jrs.1581.
- [17] P. Dillmann, F. Mazaudier, S. Hœrlé, Advances in understanding atmospheric corrosion of iron. I. Rust characterisation of ancient ferrous artefacts exposed to indoor atmospheric corrosion, *Corros. Sci.* 46 (2004) 1401–1429. doi:10.1016/j.corsci.2003.09.027.

- [18] D. De de la Fuente, I. Díaz, J. Simancas, B. Chico, M. Morcillo, Long-term atmospheric corrosion of mild steel, *Corros. Sci.* 53 (2011) 604–617. doi:10.1016/j.corsci.2010.10.007.
- [19] M. Jacot-Guillarmod, O. Rozenbaum, V. L'Hostis, P. Dillmann, D. Neff, C. Gervais, Degradation mechanisms of reinforcing iron rebars in monuments: the role of multiscale porosity in the formation of corrosion products investigated by X- ray tomography, *J. Anal. At. Spectrom.* 30 (2015) 580–587. doi:10.1039/c4ja00388h.
- [20] E. Maire, P.J. Withers, Quantitative X-ray tomography, *Int. Mater. Rev.* 59 (2014) 1–43. doi:10.1179/1743280413Y.0000000023.
- [21] S.W.T. Price, K. Geraki, K. Ignatyev, P.T. Witte, A.M. Beale, J.F.W. Mosselmans, In Situ Microfocus Chemical Computed Tomography of the Composition of a Single Catalyst Particle during Hydrogenation of Nitrobenzene in the Liquid Phase, *Angew. Chemie - Int. Ed.* 54 (2015) 9886–9889. doi:10.1002/anie.201504227.
- [22] D. Watkinson, M. Rimmer, Z. Kasztovszky, Z. Kis, B. Maróti, L. Szentmiklósi, The Use of Neutron Analysis Techniques for Detecting The Concentration And Distribution of Chloride Ions in Archaeological Iron, *Archaeometry.* 56 (2014) 841–859. doi:10.1111/arcm.12058.
- [23] K. Haneca, K. Deforce, M.N. Boone, D. Van Loo, M. Dierick, J. Van Acker, J. Van Den Bulcke, X-ray sub-micron tomography as a tool for the study of archaeological wood preserved through the corrosion of metal objects, *Archaeometry.* 54 (2012) 893–905. doi:10.1111/j.1475-4754.2011.00640.x.
- [24] A. Re, J. Corsi, M. Demmelbauer, M. Martini, G. Mila, C. Ricci, X-ray tomography of a soil block: A useful tool for the restoration of archaeological finds, *Herit. Sci.* 3 (2015) 0–6. doi:10.1186/s40494-015-0033-6.
- [25] E. Makovicky, M. Parisatto, F. Højlund, Non-Destructive Investigation of a Scalenohedral Hematite Pendant from Bahrain, c.1800 bc, *Archaeometry.* 57 (2015) 163–176. doi:10.1111/arcm.12088.
- [26] S.M. Ghahari, A.J. Davenport, T. Rayment, T. Suter, J.P. Tinnes, C. Padovani, J.A. Hammons, M. Stampanoni, F. Marone, R. Mokso, In situ synchrotron X-ray micro-tomography study of pitting corrosion in stainless steel, *Corros. Sci.* 53 (2011) 2684–2687. doi:10.1016/j.corsci.2011.05.040.
- [27] T.L. Burnett, S.A. McDonald, A. Gholinia, R. Geurts, M. Janus, T. Slater, S.J. Haigh, C. Ornek, F. Almuaili, D.L. Engelberg, G.E. Thompson, P.J. Withers, Correlative tomography, *Sci. Rep.* 4 (2014) 1–6. doi:10.1038/srep04711.
- [28] D. Johnson, J. Tyldesley, T. Lowe, P.J. Withers, M.M. Grady, Analysis of a prehistoric Egyptian iron bead with implications for the use and perception of meteorite iron in ancient Egypt, *Meteorit. Planet. Sci.* 48 (2013) 997–1006. doi:10.1111/maps.12120.

- [29] C. Chuang, D. Singh, P. Kenesei, J. Almer, J. Hryn, R. Huff, Materials Characterization Application of X-ray computed tomography for the characterization of graphite morphology in compact-graphite iron ☆, *Mater. Charact.* 141 (2018) 442–449. doi:10.1016/j.matchar.2016.08.007.
- [30] D.B. Wagner, *Science and Civilisation in China, Vol. 5: Chemistry and Chemical Technology, Part 11: Ferrous Metallurgy*, Cambridge University Press, Cambridge, 2008.
- [31] H. Cleere, D. Crossley, *The Iron Industry of the Weald*, 2nd ed., Merton Priory Press Ltd, Cardiff, 1995.
- [32] H.R. Schubert, *History of the British Iron and Steel Industry*, Routledge & Kegan Paul, London, 1957.
- [33] D. Starley, A. Hildred, Technological Examination of a Mary Rose Hailshot Piece; New Evidence for Early Gun casting, *R. Armouries Yearb.* 7 (2002) 139–146.
- [34] A. Hildred, *Weapons of Warre: The Armaments of the Mary Rose*, The Mary Rose Trust Ltd, Exeter, 2011.
- [35] L. Selwyn, Overview of archaeological iron: the corrosion problem, key factors affecting treatment, and gaps in current knowledge, *Proc. Met.* 2004. (2004) 294–306.
- [36] V. Argyropoulos, J.-J. Rameau, F. Dalard, C. Degrigny, Testing Hostacor IT as a corrosion inhibitor for iron in polyethylene glycol solutions, *Stud. Conserv.* 44 (1999) 49–57. doi:10.1179/sic.1999.44.1.49.
- [37] L.S. Selwyn, W.R. Mckinnon, V. Argyropoulos, Models for Chloride Ion Diffusion in Archaeological Iron, *Stud. Conserv.* 46 (2001) 109–120.
- [38] N.A. North, C. Pearson, Alkaline sulfite reduction treatment of marine iron, in: *Icom Comm. Conserv. 4th Trienn. Meet. Venice, 13-18 October. Prepr.*, International Council of Museums, 1975: pp. 75131–75133.
- [39] M. Drakopoulos, T. Connolley, C. Reinhard, R. Atwood, O. Magdysyuk, N. Vo, M. Hart, L. Connor, B. Humphreys, G. Howell, S. Davies, T. Hill, G. Wilkin, U. Pedersen, A. Foster, N. De Maio, M. Basham, F. Yuan, K. Wanelik, I12: the Joint Engineering , Environment and Processing (JEEP) beamline at Diamond Light Source, *J. Synchrotron Radiat.* 22 (2017) 828–838. doi:10.1107/S1600577515003513.
- [40] R.C. Atwood, A.J. Bodey, S.W.T. Price, M. Basham, M. Drakopoulos, A high-throughput system for high-quality tomographic reconstruction of large datasets at Diamond Light Source, *R. Soc. Philosophical Trans. A.* 373 (2015) 20140398.
- [41] J. Schindelin, I. Arganda-Carreras, E. Frise, V. Kaynig, M. Longair, T. Pietzsch, S. Preibisch, C. Rueden, S. Saalfeld, B. Schmid, J.-Y. Tinevez, D.J. White, V. Hartenstein, K. Eliceiri, P. Tomancak, A. Cardona, Fiji: an open-source platform for biological-image

- analysis., *Nat. Methods.* 9 (2012) 676–82. doi:10.1038/nmeth.2019.
- [42] A. Limaye, *Drishti: a volume exploration and presentation tool*, Proc. SPIE 8596, Dev. X-Ray Tomogr. VIII 85060X. (2012). doi:10.1117/12.935640.
- [43] S.P. Thompson, J.E. Parker, J. Potter, T.P. Hill, A. Birt, T.M. Cobb, F. Yuan, C.C. Tang, *Beamline I11 at Diamond: A new instrument for high resolution powder diffraction*, *Rev. Sci. Instrum.* 80 (2009) 075107. doi:10.1063/1.3167217.
- [44] A. Altomare, N. Corriero, C. Cuocci, A. Falcicchio, A. Moliterni, R. Rizzi, *QUALX2.0: A qualitative phase analysis software using the freely available database POW-COD*, *J. Appl. Crystallogr.* 48 (2015) 598–603. doi:10.1107/S1600576715002319.
- [45] C.R. Hubbard, E.H. Evans, D.K. Smith, *The reference intensity ratio, I / I_c, for computer simulated powder patterns*, *J. Appl. Crystallogr.* 9 (1976) 169–174. doi:10.1107/S0021889876010807.
- [46] R.F. Tylecote, *Metallurgy in archaeology: a prehistory of metallurgy in the British isles*, Edward Arnold Ltd, London, 1962.
- [47] M. Fontana, *Corrosion Engineering*, 3rd Ed., McGraw-Hill, 1986.
- [48] *ASM Handbook: Volume 15 Casting*, ASM International, 1992.
- [49] *ASM Handbook: Volume 13 Corrosion*, ASM International, 1992.
- [50] D. Jones, *Principles and Prevention of Corrosion*, 2nd Ed., Prentice Hall, NJ, 1992.
- [51] S.R. Freeman, *Graphitic corrosion - don't forget about buried cast iron pipes*, *Mater. Perform.* 38 (1999) 68–9.
- [52] Y.S. Shepalev, L.F. Rudenko, *Mechanism of Gray Cast Iron Corrosion*, *Fiz. Mekhanika Mater.* 14 (1978) 102–103.
- [53] A. Turnbull, *Impact of Graphite Gasket / Duplex Stainless Steel Couples on Crevice Chemistry and the Likelihood of Crevice Attack in Seawater*, *Corrosion.* 55 (1999) 206–212.
- [54] L.B. Coelho, M. Taryba, M. Alves, M.F. Montemor, M. Olivier, *Unveiling the effect of the electrodes area on the corrosion mechanism of a graphite - AA2024-T3 galvanic couple by localised electrochemistry*, *Electrochim. Acta.* 277 (2018) 9–19. doi:10.1016/j.electacta.2018.04.187.
- [55] E. Håkansson, J. Hoffman, P. Predecki, M. Kumosa, *The role of corrosion product deposition in galvanic corrosion of aluminum / carbon systems*, *Corros. Sci.* 114 (2017) 10–16. doi:10.1016/j.corsci.2016.10.011.
- [56] R.S. Sellers, W. Cheng, B.C. Kelleher, M.H. Anderson, C. Wang, T.R. Allen, R.S. Sellers, W. Cheng, B.C. Kelleher, M.H. Anderson, K. Sridharan, C. Wang, T.R. Allen, S. Steel, *Corrosion of 316L Stainless Steel Alloy and Hastelloy-N Superalloy in Molten Eutectic LiF-NaF- KF Salt and Interaction with Graphite*, *Nucl. Technol.* 188 (2014) 192–199. doi:10.13182/NT13-95.

- [57] K. Ståhl, K. Nielsen, J. Jiang, B. Lebech, J.C. Hanson, P. Norby, J. van Lanschot, On the akaganéite crystal structure, phase transformations and possible role in post-excavational corrosion of iron artifacts, *Corros. Sci.* 45 (2003) 2563–2575. doi:10.1016/S0010-938X(03)00078-7.
- [58] R. Cornell, U. Schwertmann, *The Iron Oxides: Structure, Properties, Reactions, Occurrences and Uses*, 2nd ed., Wiley-VCH Verlag GmbH & Co. KGaA, Weinheim, Germany, 2003.
- [59] S. Reguer, F. Mirambet, E. Dooryhee, J. Hodeau, P. Dillmann, P. Lagarde, Structural evidence for the desalination of akaganéite in the preservation of iron archaeological objects, using synchrotron X-ray powder diffraction and absorption spectroscopy, *Corros. Sci.* 51 (2009) 2795–2802. doi:10.1016/j.corsci.2009.07.012.
- [60] F. Kergourlay, C. Rémazeilles, D. Neff, E. Foy, E. Conforto, E. Guilminot, S. Reguer, Mechanisms of the dechlorination of iron archaeological artefacts extracted from seawater, *Corros. Sci.* 53 (2011) 2474–2483. doi:10.1016/j.corsci.2011.04.003.

Scheme 1 Structure of corrosion inhibitor Hostacor IT used in shot conservation treatment.

Fig. 1 *Mary Rose* shot number 81A6143 **a**: remaining metal core and flaked off fragments and **b**: fragment used for μ -CT; **c**: sketch of the fragmentation process.

Fig. 2 A reconstructed tomographic slice, with insets showing microstructure detail in the inner and outer areas of the fragment.

Fig. 3 Change in corrosion spot area with depth into casting; **a** outline of all corrosion spots included in the analysis and **b** change in area with distance from wax coating (green line = linear regression fit). Pink and yellow arrows indicate spots removed from scatter plot due to not representing a corroded area. The yellow arrow was used to determine the y co-ordinate of the wax layer. All distances are taken with respect to this location.

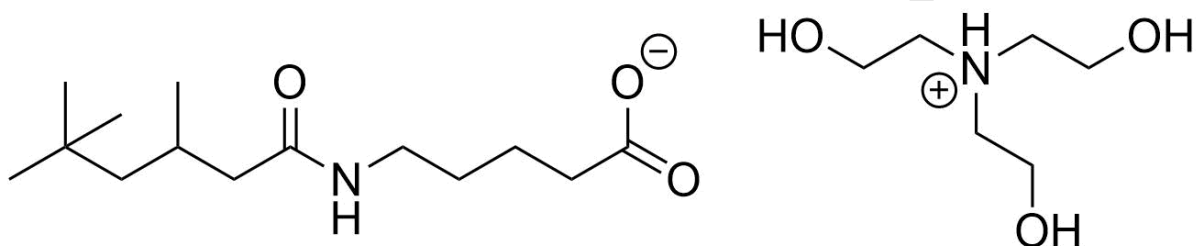
Fig. 4 Backscattered Scanning Electron Microscopy images of the corrosion spots at **a** 50x and **b** 200x magnification, with graphite flakes visible throughout all corrosion spots. Light grey = metallic matrix (pearlite + cementite), mid grey = corrosion and dark grey = graphite.

Fig. 5 3D reconstruction of tomography data, slicing through the sample (see **Fig. 1-b**) from the applied wax coating (**top left**) to the edge of the sample which had once been in contact with the rest of the object (**bottom right**). Light brown shade corresponds to the metallic areas of the sample, while dark brown spots represent the corrosion products and cracks can be seen in black. Sample height ~8 mm, for more see **SI Movie 3**.

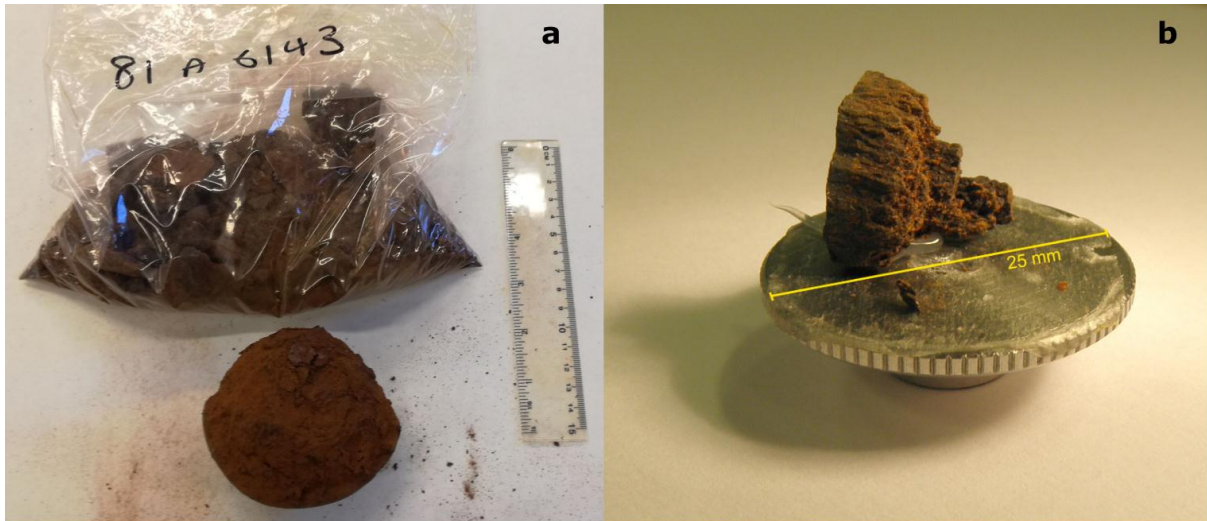
Fig. 6 Volume segmentation of different features present in the 3D tomography data. The volumes of interest are shown in **a** across the whole sample, section 1 (outer region), section 2 (middle region) and section 3 (internal region) with false colour for the metal (grey), cracks (pink), corrosion (blue) and wax (green). The corresponding volume percentages of each feature are shown per region in **b**. Ticks indicate estimated uncertainty in the segmentation procedure.

Fig. 7 SXPD of a fragment of shot 81A6143 (**green**) showing ICSD database patterns for cementite, 99017 (**light grey**), graphite, 31829 (**dark grey**) and akaganeite, 69606 (**red**). Inset shows the semi-quantitative phase proportions calculated using the *QUALX2* software.

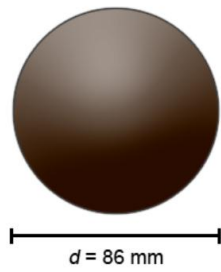
Fig. 8 Cl k-edge XANES of **a**: akaganeite standards (data from [14]) and **b**: *Mary Rose* samples. For comparison the sample from this investigation (81A6143, green) has been plotted with a washed akaganeite from another *Mary Rose* shot, see [14]. Insets show zoom-in of pre-edge feature.



Hostacor IT



c Whole cannonball at excavation



Conservation
and storage
→
Cracking

Smaller central core and fragments
from outer layer

